Published in "Journal of Physics: Condensed Matter 29 (49): 495601, 2017"
which should be cited to refer to this work.

Structural, magnetic and electronic properties of pulsed-laser-deposition grown $SrFeO_{3-\delta}$ thin films and $SrFeO_{3-\delta}$/$La_{2/3}Ca_{1/3}MnO_3$ multilayers

E Perret[1], K Sen[1], J Khmaladze[1], B P P Mallett[1], M Yazdi-Rizi[1], P Marsik[1], S Das[1], I Marozau[1], M A Uribe-Laverde[1,7], R de Andrés Prada[1,2], J Strempfer[3], M Döbeli[4], N Biškup[5], M Varela[5], Y-L Mathis[6] and C Bernhard[1]

[1] University of Fribourg, Department of Physics and Fribourg Center for Nanomaterials, Chemin du Musée 3, CH-1700 Fribourg, Switzerland
[2] Department of Physics, Stockholm University, Albanova University Center, SE-10691 Stockholm, Sweden
[3] Deutsches Elektronen-Synchrotron, Notkestraße 85, DE-22607 Hamburg, Germany
[4] Laboratory of Ion Beam Physics, ETH Zurich, Otto-Stern-Weg 5, CH-8093 Zurich, Switzerland
[5] Departamento de Física de Materiales, Facultad de Físicas and Instituto Pluridisciplinar, Universidad Complutense de Madrid, Spain
[6] Synchrotron Facility ANKA, Karlsruhe Institute of Technology, D-76344 Eggenstein—Leopoldshafen, Germany

E-mail: edith.perret@unifr.ch and christian.bernhard@unifr.ch

Abstract

We studied the structural, magnetic and electronic properties of $SrFeO_{3-\delta}$ (SFO) thin films and $SrFeO_{3-\delta}$/$La_{2/3}Ca_{1/3}MnO_3$ (LCMO) superlattices that have been grown with pulsed laser deposition (PLD) on $La_{0.3}Sr_{0.7}Al_{0.65}Ta_{0.35}O_3$ (LSAT) substrates. X-ray reflectometry and scanning transmission electron microscopy (STEM) confirm the high structural quality of the films and flat and atomically sharp interfaces of the superlattices. The STEM data also reveal a difference in the interfacial layer stacking with a SrO layer at the LCMO/SFO and a LaO layer at the SFO/LCMO interfaces along the PLD growth direction. The x-ray diffraction (XRD) data suggest that the as grown SFO films and SFO/LCMO superlattices have an oxygen-deficient $SrFeO_{3-\delta}$ structure with I4/ mmm space group symmetry ($\delta \leqslant 0.2$). Subsequent ozone annealed SFO films are consistent with an almost oxygen stoichiometric structure ($\delta \approx 0$). The electronic and magnetic properties of these SFO films are similar to the ones of corresponding single crystals. In particular, the as grown $SrFeO_{3-\delta}$ films are insulating whereas the ozone annealed films are metallic. The magneto-resistance effects of the as grown SFO films have a similar magnitude as in the single crystals, but extend over a much wider temperature range. Last but not least, for the SFO/LCMO superlattices we observe a rather large exchange bias effect that varies as a function of the cooling field.

Keywords: thin films and multilayers, complex oxides, $SrFeO_3$, magnetism, exchange bias

[7] Present affiliation: Applied Physics and Mathematics Group, Faculty of Engineering, Universidad de La Sabana, Chía, Colombia

1. Introduction

Perovskite oxides ABO_3 exhibit a strong coupling between the charge, orbital, spin and lattice degrees of freedom which gives rise to various kinds of competing interactions and nearly degenerate ground states. A prominent example is the colossal magneto-resistance effect in manganites like $LaCaMnO_3$ (LCMO) which arises from the competition between Jahn–Teller distortions, which tend to localize the charge carriers, and the so-called double-exchange interaction which gives rise to an itinerant ferromagnetic (FM) state [1, 2].

In thin films, these different ground states can also strongly depend on the strain due to the lattice mismatch between the substrate and film, which can also cause defects, like dislocations and cation or oxygen vacancies. This calls for a detailed investigation of the structural properties of such thin films. For example, LCMO thin films tend to have a reduced Curie temperature of about 190–220 K and a somewhat lower magnetic moment of about 2.5 to 3.0 μ_B per Mn [3] as compared to the bulk values of $T_c = 270$ K and 3.7 μ_B per Mn ion [4]. Furthermore, a suppression of the FM moment is commonly observed for the first few monolayers at the surface to the ambient or at the interface to the substrate or another material [5, 6].

The possibility to combine different perovskite oxides in the form of heterostructures and superlattices is also subject of great current interest. New properties, that are not inherent to the individual materials, arise at such interfaces. Prominent examples are the two-dimensional electron gas in heterostructures from the insulators $LaAlO_3$ and $SrTiO_3$ or the two-dimensional ferromagnetic order at the interface between the antiferromagnetic (AF) Mott–Hubbard insulator $LaMnO_3$ and the AF insulator $SrMnO_3$. Another interesting example is the occurrence of a FM order and a large and strongly variable exchange bias effect in $LaMnO_3/LaNiO_3$ multilayers where the latter is a paramagnetic metal in the bulk state. Usually, this exchange bias, which has attracted great interest due to its potential applications in spin-valves for quantum spintronic devices [7], occurs in multilayers of AF and FM materials for which the FM Curie temperature, T_c, is higher than the Néel temperature of the AFM, T_N. The exchange bias, H_{ex}, measures the shift of the hysteresis loop of the magnetization along the magnetic field axis which occurs after the sample has been cooled below T_N in a finite magnetic field. It results from the coupling of the magnetic moments at the AFM/FM interface that is also known as the exchange anisotropy.

Here, we present a study of the structural, electronic and magnetic properties of multilayers from LCMO and $SrFeO_{3-\delta}$ that, to our best knowledge, have not been investigated yet. $SrFeO_3$ is formally isoelectronic to $LaMnO_3$. However, unlike the Mott–Hubbard insulator $LaMnO_3$, stoichiometric $SrFeO_3$ is metallic and exhibits a helical magnetic order with a Néel-temperature of about 130 K. This marked difference arises from the much stronger hybridization with the oxygen orbitals in $SrFeO_3$ as compared to the manganites. The properties of bulk SFO are still highly variable since it tends to be strongly oxygen deficient and a special annealing treatment in high pressure oxygen or ozone atmosphere is required to obtain a fully oxidized sample. Stoichiometric $SrFeO_3$ is a cubic metal with $T_N \approx 130$ K and a second magnetic transition around 60 K that gives rise to a different helicity, which does not seem to be associated with a structural change [8, 9]. Oxygen deficient $SrFeO_{3-\delta}$ single crystals are insulating at low temperatures. In the range $\delta \leqslant 0.23$ various magnetic, charge order, and structural transitions have been identified with neutron diffraction [9]. The oxygen vacancy ordered structures at $\delta \leqslant 0.15$ also have two AF transitions at 130 K and 75 K. However, unlike in $SrFeO_3$, the second AF transition is accompanied by a charge order (CO) and a structural transition from a tetragonal into a monoclinic state. For the more strongly oxygen deficient $SrFeO_{2.81}$ this second AF/CO transition to a monoclinic structure is reduced to about 62 K [10]. Finally, $SrFeO_{2.77}$ exhibits three AF transitions at 232 K, 110 K and 65 K with no sign of a concomitant CO or structural transition [9].

There are only few publications that discuss the growth and the physical properties of stoichiometric as well as oxygen-deficient SFO thin films [11–17]. In the following we therefore present first a detailed description of the growth and the characterization of the bare SFO thin films in the as-grown and the ozone annealed states, before we proceed to the corresponding SFO/LCMO multilayers.

The utilized experimental techniques, like pulsed laser deposition (PLD), x-ray diffraction (XRD), x-ray reflectivity (XRR), Rutherford backscattering spectroscopy (RBS), scanning transmission electron microscopy (STEM), transport and magnetization measurements and infrared ellipsometry are described in section 2. The discussion of the structural, magnetic, and electronic properties of SFO thin films is presented in sections 3.1.1–3.1.3 and of SFO/LCMO multilayers in sections 3.2.1–3.2.3, respectively.

2. Experiment

2.1. Pulsed laser deposition

The SFO thin films and SFO/LCMO multilayers have been grown on single crystal (0 0 1)-oriented substrates with pulsed laser deposition (PLD) using an excimer KrF laser ($\lambda = 248$ nm, $t_s = 25$ns). The laser beam spot had a size of about 3 mm^2. For the deposition we have used a repetition rate of 2 Hz for all depositions and a fluency between 1.5 and 2.0 J cm^{-2}. The substrates with different pseudo-cubic lattice parameters; $La_{0.3}Sr_{0.7}Al_{0.65}Ta_{0.35}O_3$ (LSAT), $SrTiO_3$ (STO, $a = 3.905$ Å) and $LaAlO_3$ (LAO) were purchased from Crystec and were placed 5 cm above the targets. Literature values of the pseudo-cubic lattice parameter of LSAT [18, 19] $a_{LSAT} = 3.872$ Å and of $a_{LAO} = 3.789$ Å [20, 21] are in good agreement with our x-ray diffraction measurements ($a_{LSAT} = 3.873$ Å, $a_{LAO} = 3.793$ Å).

The substrates were heated with a rate of 15 °C min^{-1} to the deposition temperature (800 °C) using an infrared laser. The partial pressure of the oxygen gas was set to 0.11 mbar during the deposition. After the growth, the chamber was

vented with oxygen and the sample was cooled to 550 °C at a rate of 5 °C min^{-1} and *in situ* annealed for one hour at 550 °C followed by a rapid cooling step to room temperature with 30 °C min^{-1}.

2.2. Ozone annealing

Ex situ ozone annealing was performed with a laboratory ozonizer from Erwin Sander GmbH. The samples were heated in an ozone flow of 1.5 Nl h^{-1} to 200 °C in 30 min and were kept at this temperature for about 6 h 30 min. After subsequent cooling to room temperature the ozone flow was turned off when the sample reached about 50 °C. The total ozone annealing time amounted to 8 h.

2.3. X-ray diffraction and reflectivity

Synchrotron x-ray diffraction has been performed on a SFO/LCMO superlattice at the P09 beamline at PETRA III synchrotron at DESY, Germany. The x-ray energy was 6.869 keV, just below the Fe K-edge, to avoid fluorescence background. Other x-ray diffraction and reflectivity measurements have been performed with a four-circle diffractometer (Rigaku SmartLab). The instrument is equipped with a 9 kW rotating Cu-Kα_1 anode and the incident parallel beam optics consist of a reflecting mirror and a two-bounce Ge (2 2 0) monochromator ($\Delta\lambda/\lambda = 3.8 \times 10^{-4}$). A scintillation counter was used as a detector. Out-of-plane lattice parameters have been deduced from the fourth pseudo-cubic Bragg peaks (0 0 4) from $2\Theta - \omega$ scans, by applying Bragg's law. In-plane lattice parameters were derived from the reciprocal space maps (RSM) around the pseudo-cubic (0 2 4) Bragg peak. The monochromator was removed for the measurements of weak half-order peaks.

2.4. Transport and magnetization measurements

Resistance and magnetization measurements were performed with a Quantum Design PPMS 9 T system. The 4-point probe technique was used to measure the resistance. The samples were fixed onto a sample puck with a double-sided tape and four copper wires were glued onto the corners of the samples using silver paste. A fixed DC-current of typically 10 μA was applied and the voltage was measured. For strongly insulating samples, we have used a Keithley 2602 digital multi-meter to measure the current from a set DC voltage. The temperature dependence of the resistance was measured using a ramping rate of either 2 K min^{-1} or 4 K min^{-1}. The magnetic moment was measured with a vibrating sample magnetometer (VSM). The magnetic field was applied parallel to the film surface, with the samples being fixed onto a quartz holder using UHU-glue. The temperature dependence of the magnetic moment was recorded during field cooling with a ramping rate of 2 K min^{-1}. M–H loops were measured after field cooling to 10 K and subsequent heating in field to the temperature of interest. The magnetic field was sweeped at a rate of 11 Oe s^{-1} during M–H loops. The raw data were corrected for the paramagnetic and diamagnetic response of the substrate by fitting a Brillouin function plus a diamagnetic contribution to the data, in order to extract the magnetism of the thin films.

2.5. Rutherford backscattering spectroscopy

The chemical composition of the films was analyzed by Rutherford backscattering spectrometry (RBS) [22, 23] at the ETH Laboratory of Ion Beam Physics, Switzerland. Monolayers of SFO and LCMO were deposited onto MgO ($a = 4.212$ Å) single crystals using the same deposition procedure as for the epitaxially strained films on other substrates. Measurements were performed using a 2 MeV 4He beam and a silicon PIN diode detector under 168 degree. The collected RBS data were analyzed using RUMP code simulations [24]. For the SFO films they confirmed the 1:1 ratio of the Sr and Fe ions. For the ozone annealed samples they indicated a minor contamination with Ag and Cl. The LCMO layers were found to be slightly Ca-deficient with a cation ratio of La0.71:Ca0.29:Mn0.98. The experimental uncertainty of the RBS analysis for the ratio of the cation concentrations is about $\pm$1–2%. For the lighter oxygen ions the values are not quoted since the error is even larger, i.e. on the order of $\pm$5%.

2.6. Ellipsometry

The temperature and frequency dependent optical response has been determined with spectroscopic ellipsometry. We have used a home-built setup attached to a Bruker 66 v FTIR spectrometer at the IR beamline of the ANKA synchrotron source and to a Bruker 113 v FTIR spectrometer with an internal mercury arc light source to measure the response of two thick SFO thin films in the far-infrared (70–700 cm^{-1}) and mid-infrared (500–4500 cm^{-1}) ranges, respectively [25]. A rotating analyzer scheme with and without a Si-prism compensator was used in the far-infrared and a ZnSe-prism based rotating compensator in the mid-infrared. The effective response of the SFO layer has been obtained by fitting the data with a standard optical transfer matrix model (substrate/film/ambient) in a point-by-point manner. As input parameters we used the dielectric function of a reference LSAT substrate as measured with ellipsometry and the film thickness as obtained from the x-ray reflectivity fits.

2.7. Transmission electron microscopy

Cross-sectional high-resolution scanning transmission electron microscopy (STEM) images of the superlattices were acquired in an aberration-corrected JEOL JEM-ARM200 CF operated at 200 kV, and equipped with a Gatan Quantum electron energy-loss spectrometer (EELS). All images were obtained using a high-angle annular dark field (ADF) detector. The technique is also known as *Z*-contrast imaging. For this technique, the intensity of every atomic column is approximately proportional to the square of the atomic number, Z^2. EELS elemental mapping was performed by integrating the signals under the characteristic elemental edges after

Table 1. List of characterized SFO samples.

Label	Samples	Techniques
M1/M1[a]	STO-SFO (33 nm)	XRR, XRD
M2/M2[a]	LSAT-SFO (33 nm)	XRR, XRD, 4-point probe
M3/M3[a]	LAO-SFO (33 nm)	XRR, XRD
M4/M4[a]	LSAT-SFO (109–114 nm)[b]	XRR, RSM, 4-point probe, Ellipsometry, VSM
M5	LSAT-SFO (25 nm) -LAO (2 nm)	XRR, STEM

[a] Ozone annealed samples.
[b] Thickness range of duplicate samples.

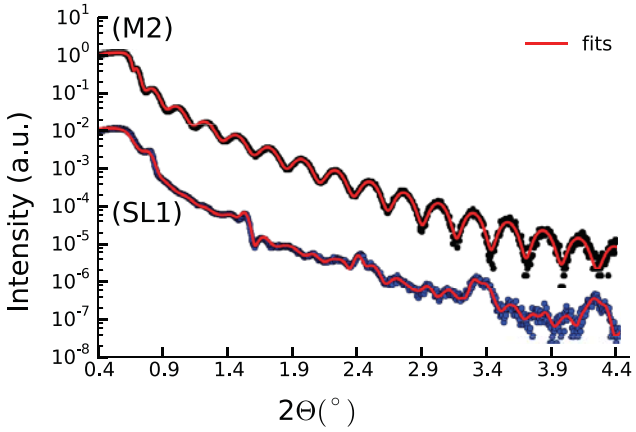

Figure 1. X-ray reflectivity of a SFO monolayer (M2) and a $[SFO/LCMO]_{10}$-LAO superlattice (SL1) grown on LSAT. Best fits are shown as solid red lines.

background subtraction using a power law. The integration windows were around 20–30 eV wide. Random noise was removed by means of principal component analysis [26]. The specimens were prepared by conventional methods of grinding and Ar-ion milling.

3. Results and discussions

The properties of single SFO thin films are discussed in the next section 3.1 and the ones of SFO/LCMO multilayers in subsection 3.2.

3.1. $SrFeO_{3-\delta}$ thin films

A list of the studied $SrFeO_{3-\delta}$ thin film samples, their annealing treatment, thicknesses as well as the applied characterization techniques is given in table 1. The samples M1–M3 were grown on different substrates (STO, LSAT, LAO) in order to study the effect of ozone annealing on the differently strained SFO films. Thicker SFO films (about 100 nm) grown on LSAT (M4), with an enhanced signal strength from the SFO film as opposed to thinner films (about 30 nm), were used to measure the reciprocal space maps (RSM), optical conductivity and magnetization. The magnetoresistance was measured on thin (M2) and thick SFO films (M4) grown on LSAT. To speed up the measurements with the various kinds of characterization techniques, we have used duplicate samples. An additional sample (M5) with a LAO protection layer was used for characterization with STEM.

3.1.1. Structural properties. We used the following techniques to determine the structural properties of the SFO thin films. With XRR we determined the film thicknesses and roughnesses (section 3.1.1.1), XRD was used to study the effect of ozone-annealing on the differently strained films (section 3.1.1.2), the epitaxy was studied with RSM (section 3.1.1.3) and the atomic structure with STEM (section 3.1.1.4).

3.1.1.1. Determination of layer thickness with XRR. The thickness of the films has been obtained by fitting the x-ray reflectivity (XRR) curves with the GenX software [27]. As an example, figure 1 shows the data and fits of the XRR curve of a SFO film (M2) and a SFO/LCMO superlattice (SL1). The best fit of the SFO film (M2) yields a total thickness of $d = 32.8$ nm and a rms roughness of 0.6 nm.

3.1.1.2. Strain and ozone-annealing effects with XRD. Figure 2 displays the x-ray diffraction curves around the pseudo-cubic (004) Bragg peak of the SFO thin films M1-M3 with a thickness of 33 nm that have been grown on STO, LSAT and LAO substrates, respectively. The solid lines show the result in the as grown state after *in situ* annealing in 1 bar of oxygen and the dotted lines after *ex situ* annealing in ozone atmosphere. The nominal lattice mismatch between SFO and the substrate amounts to $+1.4\%$ for STO (tensile strain), $+0.6\%$ for LSAT (tensile strain) and -1.6% for LAO (compressive strain).

It is expected that the *ex situ* ozone annealing step reduces the concentration of the oxygen vacancies in SFO and leads to a decrease of the out-of-plane lattice parameter and a corresponding shift of the SFO (004) Bragg peak toward higher scattering angles. Nevertheless, figure 2 shows that the expected upward shift of the (004) Bragg peak upon ozone annealing occurs only for the SFO film on LSAT but not for the STO and LAO substrates. For the latter, the ozone annealing step rather causes a broadening of the Bragg peak which indicates a reduced crystallinity. The disappearance of satellite peaks for the STO/SFO samples also indicates an increased roughness of the sample surface.

These findings suggest that the lattice mismatch between the SFO thin film and the substrate, which is larger for LAO and STO than for LSAT, precludes the inclusion of oxygen during the ozone annealing.

XRD peak positions of the pseudo-cubic SFO film grown on STO are very close to peak positions found by Hirai *et al*, for which a stoichiometry of $SrFeO_{2.8}$ was obtained with Mössbauer spectroscopy [14].

These XRD results demonstrate that the ozone annealing step allows one to oxygenate SFO thin films that are grown on substrates with a fairly small lattice mismatch, like LSAT. In the following we are therefore focusing on the SFO films grown on LSAT.

For SFO on LSAT (M2) the out-of-plane lattice parameter decreases from $c = 3.848$ Å in the as grown state to 3.840 Å after ozone annealing, corresponding to a change of

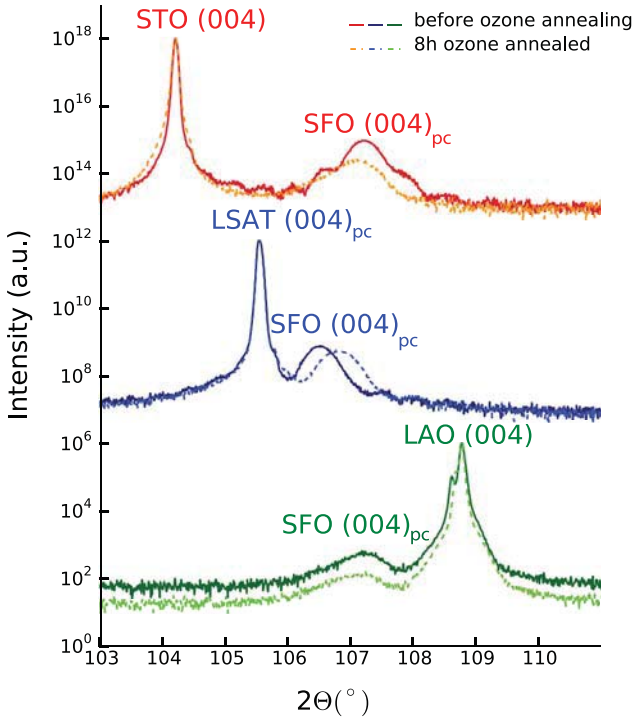

Figure 2. X-ray diffraction curves around the pseudo-cubic (004) Bragg peak of SFO thin films (M1-M3) on three different substrates (top: STO, centre: LSAT, bottom: LAO).

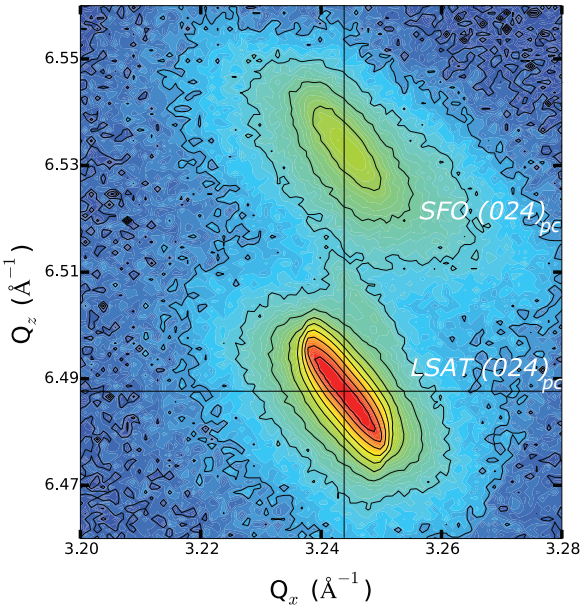

Figure 3. Reciprocal space maps around the pseudo-cubic (024) Bragg peak of a 109 nm thick SFO film grown on LSAT (M4).

-0.21%. A similar lattice parameter of $c = 3.837$–3.840 Å was previously reported for *in situ* ozone annealed SFO films and has been assigned to stoichiometric $SrFeO_3$ [11, 16, 17]. Additionally, fully strained $SrFeO_{2.5}$ thin films on LSAT have been found to have an out-of-plane lattice parameter of 4 Å [16]. The small change in the out-of-plane lattice parameter from the as grown state to ozone-annealed state of the SFO monolayer (M2) suggests that the as-grown film has a rather small oxygen deficiency ($\delta < 0.2$).

3.1.1.3.Epitaxy with RSM. Figure 3 shows a reciprocal space map of the x-ray scattering around the pseudo-cubic LSAT (024) Bragg peak for an as grown, epitaxial SFO film (M4) with a thickness of 109 nm. It confirms that the SFO film grows fully strained on the LSAT substrate and has a tetragonal structure with in-plane and out-of-plane lattice parameters of aSFO = aLSAT = 3.874 Å and cSFO = 3.847 Å, respectively.

3.1.1.4.Atomic structure with STEM. Figure 4 shows the STEM images of the as grown $SrFeO_{3-\delta}$ thin film M5 with $d = 25$ nm that is capped with a 2 nm thick $LaAlO_3$ protection layer. These are high angle annular dark field (HAADF) images where the heavier atoms appear brighter than the lighter ones. Dark stripes that run either perpendicular or parallel to the surface of the SFO layer are observed in both the medium (figure 4(a)) and high (figure 4(b)) magnification images. The horizontal (vertical) stripes are rows with dilated unit cells in the vertical (horizontal) direction. This unit cell dilation appears in every second unit cell layer but varies in magnitude. These stripes correspond to oxygen deficient $FeO_{2-\delta}$ atomic planes. Oxygen deficiency gives rise to a local lattice expansion that yields a lower intensity of the ADF signal. Dark stripes at every second perovskite unit cell have been previously observed in brownmillerite structures, such as $SrFeO_{2.5}$ [28–30] or $La_{0.5}Sr_{0.5}CoO_{2.5}$ under epitaxial strain [31].

This finding suggests that SFO adopts an oxygen-deficient brownmillerite structure. A quantification of the average composition of the film from an analysis of the EELS edges confirms such an oxygen deficiency (figure 4(c)). The oxygen *K* edge around 531 eV and the iron $L_{2,3}$ edge near 709 eV were measured simultaneously with the STEM images. Their analysis yields an average oxygen-to-iron atomic ratio close to 2.5, i.e. well below the nominal value of 3. Nevertheless, it should be noted that the oxygen *K*-edge EELS experiment has a significant error bar of about 5–10%.

The oxygen deficiency with a composition close to $SrFeO_{2.5}$ obtained from STEM is about twice as large as the one deduced from the analysis of the XRD data. We can only speculate about the origin of this difference. For example, it may be related to the circumstance that the STEM technique probes the sample at a much more local scale than the x-ray experiment which averages over almost the entire sample. The differences between the STEM and XRD experiments thus could result from a strongly inhomogeneous spatial distribution of the oxygen vacancies. A second possibility is a loss of oxygen during the preparation of the specimen for the STEM study, especially during the ion milling. A previously reported rapid phase transformation under the electron beam [32] has not been observed during the STEM measurements and thus can be excluded.

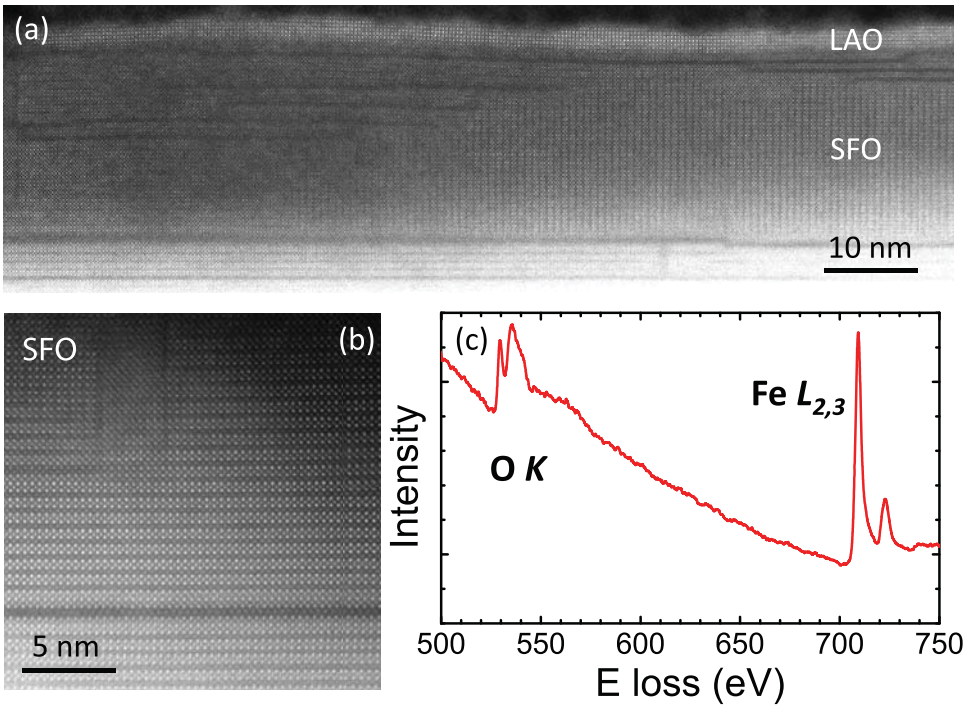

Figure 4. Medium (a) and high (b) magnification annular dark field images of a $SrFeO_{3-\delta}$ thin film on LSAT (M5). (c) Example of average oxygen K and iron $L_{2,3}$ edges measured on the $SrFeO_{3-\delta}$ films.

3.1.2. Magnetic properties. In this section we present the magnetic properties of the thick SFO film before and after ozone annealing as measured with a VSM.

3.1.2.1.DC magnetization. Figure 5 shows the temperature-dependent magnetization of the as grown film (M4, blue line) and the ozone annealed film (M4a, red line) measured during heating after field-cooling in 6 Tesla. For clarity the data of the latter have been vertically offset by 0.2 memu. From these curves we have subtracted a weak, spurious paramagnetic signal from the LSAT substrate, that has been determined with a Curie fit to the data below 40 K, as well as the diamagnetic signal of the LSAT substrate that has been obtained from a linear fit to the M–H scan at 300 K.

Once more, we find that the properties of the as grown and the ozone annealed SFO film closely resemble the ones of $SrFeO_{2.81}$ and $SrFeO_{2.95}$ crystals, respectively [8, 33]. The onset temperature of the helical order, as deduced from the decrease of the magnetization, is significantly higher for the ozone annealed film with $T_N = 124$ K than for the as grown SFO film with $T_N = 84$ K. The former is also significantly higher than in previous reports for films with a thickness of less than 50 nm for which $T_N = 110$ K [11, 16]. The ozone annealed film still shows clear signatures of a second magnetic transition around 84 K and a thermal hysteresis effect that persist to about 57 K. A similar behavior was reported for single crystalline $SrFeO_3$ [8]. The inset in figure 5 shows the MH loops measured at 10 K for the ozone-annealed sample after cooling in almost zero field (black line) and at 6 T (green line). The latter yields an enhanced magnetic moment at 10 K that is not recovered after a magnetization loop to −6 T and then back to +6 T. This training effect suggests that the magnetic-field-induced polarization of the helical spin order is strongly hysteretic.

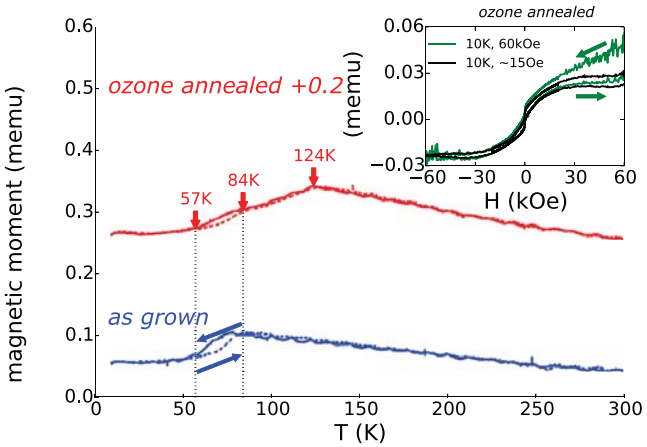

Figure 5. Magnetization versus temperature upon 6 T field cooling for duplicates of the as grown SFO film, M4 (blue line) and the ozone annealed SFO film, M4a (red line, offset by 0.2 memu). Inset: Magnetic moment versus applied magnetic field measured at 10 K after field-cooling in 6 T (green line) and about 15 Oe (black line).

3.1.3. Electronic properties. The magnetoresistance of SFO films with different thicknesses has been determined with a 4-point probe technique (section 3.1.3.1) and the optical conductivity of thick films (about 100 nm) has been measured with ellipsometry (3.1.3).

3.1.3.1.Magnetoresistance with 4-point probe. In the following we present the DC magneto-electric transport of as-grown and ozone annealed SFO films. In the as grown state we find

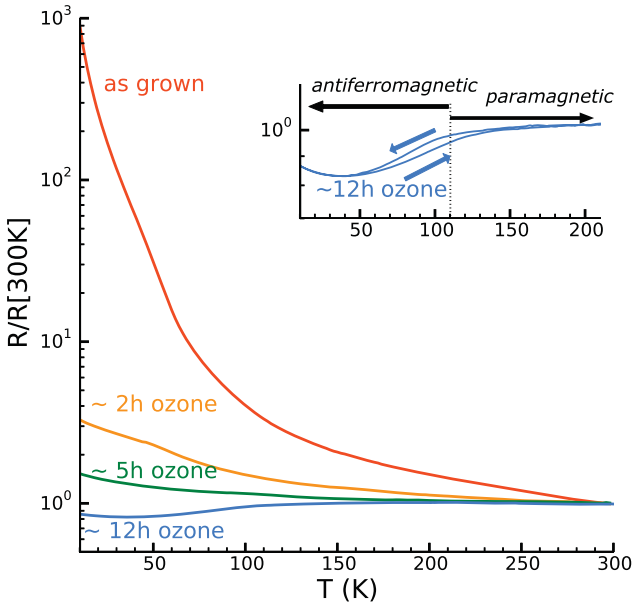

Figure 6. Temperature dependence of the DC resistance of as grown (red line, $R[300\ \mathrm{K}] = 328\Omega$), 2 h ozone-annealed (orange line, $R[300\ \mathrm{K}] = 263\Omega$), 5 h ozone-annealed (green line, $R[300\ \mathrm{K}] = 219\Omega$), and 12 h ozone-annealed (blue line, $R[300\ \mathrm{K}] = 112\Omega$) 33 nm thick SFO film (M2) on LSAT.

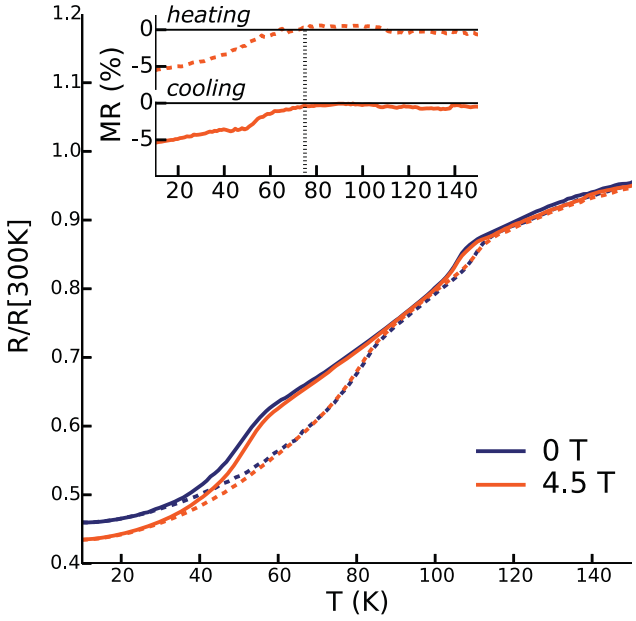

Figure 7. DC resistance in zero field and 4.5 T field cooling and heating of an ozone annealed 33 nm thick SFO film (M2a). Inset: Magnetoresistance MR $= [R(H) - R(0)]/R(0)$ for 4.5 T field cooling and heating.

that they are rather similar to the ones of tetragonal $SrFeO_{3-\delta}$ with $\delta \leqslant 0.2$ single crystals whereas in the extensively ozone annealed samples there is a good agreement with the cubic $SrFeO_3$.

Figure 6 displays the temperature dependent DC resistance of a 33 nm thick SFO film (M2) for which the oxygen content has been stepwise increased by annealing in an ozone flow of 1.5 Nl/h at 200 °C. It shows that the ozone annealing increases the conductivity of the sample and suppresses the insulator-like upturn of the resistance toward low temperature that is very prominent in the as grown state. In the final state the resistance exhibits a metal-like temperature dependence similar to the one that was reported for a $SrFeO_{2.95}$ single crystal in [8], except for a weak upturn below 50 K that is not seen in the single crystal.

The DC resistance of a duplicate SFO film (33 nm, M2a) which has been ozone annealed in one step for 8 h is shown in figure 7. The overall temperature dependence is metallic with a pronounced decrease toward low temperature. There are also pronounced thermal hysteresis effects in the temperature range between 30 and 115 K with an intermittent region around 95 K with a very small hysteresis. Similar anomalies were previously reported for a 50 nm thick SFO_3 film on LSAT that had two Néel temperatures of 46 K and 104 K [11]. These anomalies have been attributed to different helimagnetic phases with nontrivial spin structures. We find a Néel temperature of about 110 K, where a change in the slope of the zero field cooling curve is observed, in good agreement with a previous report [16].

The inset shows the magnetoresistance, MR $= [R(H) - R(0)]/R(0)$, which has been deduced from the difference between the zero-field cooled and the field-cooled resistance $R(0\ \mathrm{T})$ and $R(4.5\ \mathrm{T})$, respectively. The MR effect of about -5% at 10 K is rather small and decreases toward higher temperature where it vanishes around 75 K.

Figure 8 compares the temperature-dependent resistance and magnetoresistance curves of a 109 nm thick SFO film in the as grown state (M4) and of a 114 nm thick duplicate film after ozone annealing (M4a). In the former state the resistance exhibits a steep and strongly hysteretic upturn below about 80 K upon warming and 60 K upon cooling that is reminiscent of the behavior reported for a $SrFeO_{2.81}$ single crystal [8]. Thin (about 30 nm) SFO films typically show an increase of the resistance toward low temperature by about 3–5 orders of magnitude, which is smaller than the increase by 6–7 orders for thick (about 100 nm) SFO films. This suggests that thick SFO films contain more defects resulting in a higher resistance. The ozone annealing (8 h) did therefore not lead to a fully metallic film for the 114 nm thick SFO film, M4a.

The inset in figure 8 shows the magnetoresistance. The MR exhibits a rather sharp transition around 80 K where it suddenly changes from a positive value at higher temperature to a large negative one at lower temperature with $\mathrm{MR}(80\ \mathrm{K}) = +41\%$ and $\mathrm{MR}(10\ \mathrm{K}) = -87\%$. This positive MR at higher temperatures has not been observed for all the as grown films. Thin (about 30 nm) films just show a negative MR effect with a slight variation of the onset temperature. Such a large negative MR effect was also reported for $SrFeO_{2.85}$ single crystals with $\mathrm{MR}(70\ \mathrm{K}) = -90\%$ and $SrFeO_{2.81}$ crystals with $\mathrm{MR}(70\ \mathrm{K}) = -40\%$ and attributed to a charge-order transition. Different from our SFO thin films, this negative MR was limited to a narrow temperature range around 70 K, at low temperature the MR was either very small or even positive [8, 33]. Note that we have confirmed that these differences between the low temperature MR of the SFO thin films and the single crystals are not arising from different measurement techniques

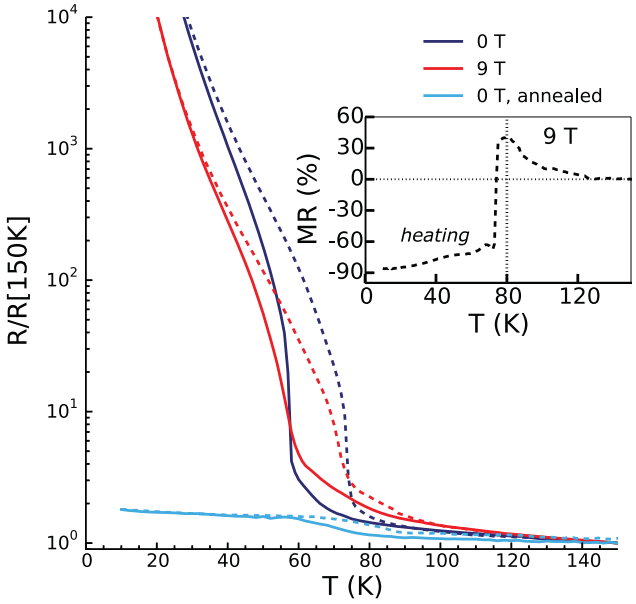

Figure 8. DC resistance in zero and 9 T field cooling (full lines) and heating (dashed lines) runs from a 109 nm thick as grown SFO film on LSAT M4, ($R[150\ \mathrm{K}] = 814\Omega$) and DC resistance of a ozone annealed 114 nm thick SFO film M4a, ($R[150\ \mathrm{K}] = 360\Omega$). Inset: Magnetoresistance MR $= [R(H) - R(0)]/R(0)$ for heating at 9 T for the as-grown sample M4.

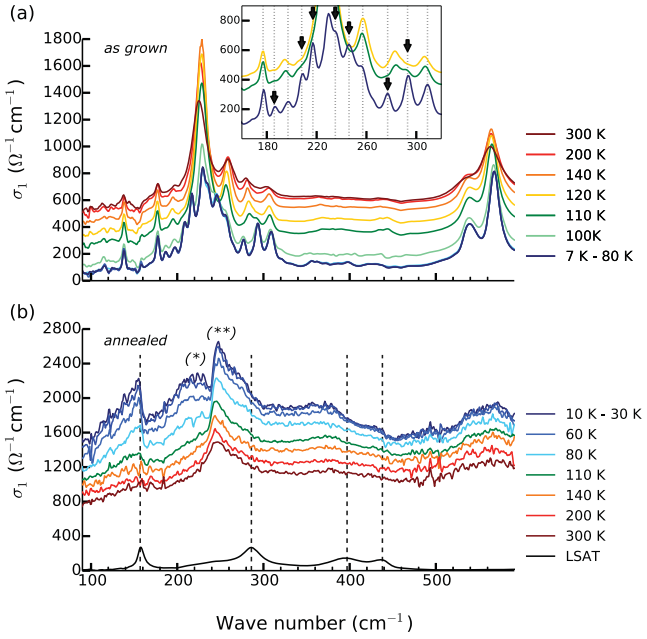

Figure 9. Substrate corrected real part of the infrared conductivity before (a) and after ozone annealing (b) of a 109 nm thick SFO film (M4/M4a) on LSAT. The conductivity was measured at various temperatures from 7 K up to 300 K.

(isothermal versus. field cooling scans). Accordingly, it seems to be related to the defects and strain effects in the thin films.

3.1.3.2.Optical conductivity with ellipsometry. Figure 9 shows the infrared conductivity of a 109 nm thick SFO film (M4/M4a) on LSAT before (a) and after ozone annealing (b). The spectra have been corrected for the substrate contribution and represent the intrinsic response of the SFO thin film. The measurements have been performed by stepwise increasing the temperature starting from 10 K. The infrared data thus should be compared with the heating branch of the resistances in figure 8 (dotted blue/cyan lines).

For the as-grown state (figure 9(a)), the electronic part of the infrared conductivity is very weak below 80 K where the resistance data in figure 8 show a highly resistive state. Above 80 K the electronic conductivity starts to increase and gives rise to a broad band with a weak maximum at 400–500 cm^{-1}. This electronic band exhibits the strongest increase between 100 and 120 K and tends to saturate above 200 K. Some of the infrared active phonon modes are also undergoing pronounced changes around 120 K. The inset in figure 9(a) shows that at least seven new phonon modes (marked by arrows) appear at low temperature. Remarkably similar infrared spectra with corresponding changes were previously observed in a $SrFeO_{2.85}$ single crystal and interpreted in terms of a transition into a charge ordered state at low temperature with an enlarged unit cell [33]. The additional infrared-active phonon modes thus can be understood in terms of a Brillouin-folding.

The electronic infrared conductivity of the ozone annealed SFO sample (figure 9(b)) is significantly larger than in the as grown state and it increases toward low temperature. The electronic response still has an unusual shape with a broad maximum around 300–400 cm^{-1} that is clearly different from a Drude-like response of itinerant carriers for which the conductivity increases toward the DC limit.

Some of the infrared-active phonon modes are also quite anomalous. Between 140 and 300 K only the three phonon modes expected for cubic $SrFeO_3$ are observed around 156, 245 and 570 cm^{-1}. Below 140 K several additional, sharp features start to develop which have a Fano-like shape [34, 35]. Most of them coincide with the phonon modes of the LSAT substrate as shown by the dotted lines.

Whereas some of these modes coincide with the phonon mode of the LSAT substrate, we can exclude that these are due to an incorrect correction of the substrate contribution to the response function (since they appear only below 140 K and some of them do not coincide with LSAT phonons). It rather seems that these resonance features are the signatures of a spatially inhomogeneous electronic response of the SFO film. For example, there may be insulating regions due to the clustering of the few oxygen vacancies that exist in these ozone annealed films (see section 3.1.3.1) that are embedded in a matrix of fully oxygenated, metallic material. The local field effect at the interfaces between the insulating and metallic regions can indeed give rise to Fano-type features in the vicinity of the phonon modes of the insulating regions [36]. The strong influence of the phonon modes of the LSAT substrate on these resonance features is still somewhat surprising. It may indicate that these oxygen deficient regions are mostly located near the LSAT substrate.

3.2. $SrFeO_{3-\delta}$—$La_{2/3}Ca_{1/3}MnO_3$ *(SFO-LCMO) multilayers*

A list of the studied $SrFeO_{3-\delta}$—$La_{2/3}Ca_{1/3}MnO_3$ multilayers and their layer thicknesses is given in table 2. The structure of the multilayer SL1 with 9 nm thick SFO and LCMO layers

Table 2. List of the SFO/LCMO multilayers and the LCMO monolayer reference.

Label	Samples	Techniques
SL1	$[SFO(9nm)\text{-}LCMO(9nm)]_{10}$-LAO(2nm)	XRR, XRD, RSM, 4-point probe, VSM
SL2	$[SFO(10nm)\text{-}LCMO(10nm)]_{10}$-LAO(2nm)	XRR, STEM
ML1	LSAT-LCMO(28nm)-LAO(3nm)	XRR, VSM

was investigated with XRD and RSM and its electronic and magnetization properties with 4-point probe and VSM measurements. The SL2 with slightly thicker SFO and LCMO layers (10 nm) was used for STEM characterization. The thin LCMO film, ML1, was measured as a reference for the electronic and magnetic properties of LCMO.

All the SFO/LCMO multilayers that are discussed in the following are in the as-grown state. The ozone-annealing of these multilayers resulted in insulating samples with a reduced structural quality, which are not further discussed here.

3.2.1. Structural properties. The structural properties of the SFO/LCMO multilayers have been investigated with different techniques. With XRR we determined the layer thicknesses and roughnesses (section 3.2.1.1), XRD was used in order to determine the oxygen deficiency and space group of SFO as well as the growth direction of LCMO (section 3.2.1.2), the epitaxy was studied with RSM (section 3.2.1.3) and the atomic structure, including the interface terminations, with STEM (section 3.2.1.4).

3.2.1.1. Determination of layer thickness from XRR. The fit of SL1 in figure 1 yields a film thickness of 9.5 nm for SFO and 9.4 nm for LCMO. The surface roughness of the SFO layers evolves from about 7–8 Å for the two topmost layers to about 3 Å for the layers below. A similar trend is observed for the LCMO layers for which the roughness decreases from 3–6 Å for the topmost layers to less than 1 Å for the lower LCMO layers. These low roughness values testify for the high quality of this superlattice.

3.2.1.2. Oxygen order with XRD. Next we discuss how the oxygen deficiency, the space group of SFO as well as the growth direction of LCMO have been deduced from the XRD data. Figure 10 shows crystal truncation rods (CTRs) along the [0 0 L] and [1 1 L] directions for the SL1. The strong reflections at integer positions correspond to the typical LSAT cubic perovskite cell with a Pm3m space group and a pseudo-cubic lattice constant of about 3.87 Å. Half-order peaks from the SL appear on the [1 1 L] CTR but are absent along [0 0 L].

As listed in table 3, additional half-order peaks have been observed at the positions 1/2(o,o,o), 1/2(e,e,o), 1/2(e,o,e), 1/2(o,e,e) and quarter-order peaks at the position 1/4(o,o,2o), with o: odd integer and e: even integer numbers. These half-order reflections originate from a doubling of the unit-cell which may be caused by (i) a tilting of the octahedra, (ii) an ordering (superstructure) of the chemical species or vacancies, or (iii) by a displacement of the cations.

The half-order reflections at the 1/2(o,o,o) positions can be assigned to the F-43m space group of the LSAT substrate with

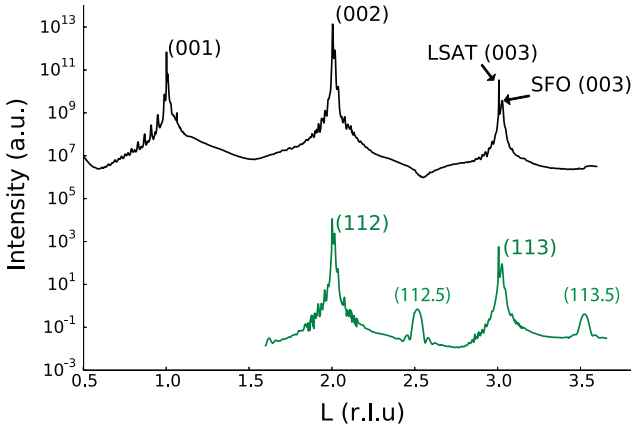

Figure 10. [0 0 L] and [1 1 L] crystal truncation rods of the $[SFO\ LCMO]_{10}$-LAO superlattice (SL1) grown on LSAT.

a lattice constant of 7.74 Å and result from a superstructure (scenario ii) due to an ordering of the Al and Ta ions [37, 38]. These reflections are also observed for a bare LSAT substrate and are therefore not specific to the SFO/LCMO superlattices.

The half-order peaks at the 1/2(e,e,o) positions, e.g. (1,1,2.5), are attributed (within scenario i) to the orthorhombic structure of LCMO with the long-axis pointing out-of-plane.

The 1/2(e,o,e), 1/2(o,e,e) and 1/4(o,o,2o) peaks appear to be specific to the SFO layers. They cannot be explained in terms of the octahedral tilts of scenario (i) since they do not comply with the rules given by Glazer and Woodward [39, 40]. Instead, we have verified that they can be assigned to the oxygen vacancy ordering of the tetragonal structure of $SrFeO_{2.81-2.875}$ [10, 41, 42]. We have simulated the corresponding diffraction patterns for different orientations of the $SrFeO_{3-\delta}$ structures on LSAT with the Rigaku SmartLab software in order to assign the 1/2(e,o,e) and 1/2(o,e,e) reflections. The structure of $SrFeO_{2.5}$, which has the long-axis pointing out-of-plane, and $SrFeO_{2.81}$, which has the c-axis lying in-plane, would lead to half-order reflections along the [00L] CTR [30] which are not seen in figure 10. These structures can therefore be excluded. The $SrFeO_{2.5}$ structure, which has the long-axis along the in-plane direction would lead to reflections at 1/2(e,o,e) and 1/2(o,e,e) positions without half-order reflections along [00L]. The same reflections would occur for $SrFeO_{2.81-2.875}$ which has the c-axis along the out-of-plane direction. The distinction between these two structures is based on the 1/4(o,o,2o) peaks which occur only for the tetragonal $SrFeO_{2.81-2.875}$ structure. The same 1/4(o,o,2o) peaks were found for the 109 nm thick SFO film (M4).

In summary, the assignment of the x-ray diffraction data suggests that the superlattice SL1 consists of $SrFeO_{3-\delta}$ layers with a tetragonal structure, an oxygen deficiency of about

Table 3. List of the observed half-order and quarter-order Bragg peaks.

Found pseudo-cubic (HKL)	LSAT F-43m, $a = 7.74$ Å, $b = 7.74$ Å, $c = 7.74$ Å, [0 0 1]	LCMO Pnma, $a = 5.457$ Å, $b = 7.711$ Å, $c = 5.417$ Å, [0 1 0]	$SrFeO_{2.81-2.875}$ I4/mmm $a = 10.932$ Å, $b = 10.932$ Å, $c = 7.700$ Å, [0 0 1]
1/2(o,o,o)	Yes	—	—
1/2(e,e,o)	—	Yes	—
1/2(e,o,e)	—	—	Yes
1/2(o,e,e)	—	—	Yes
1/4(o,o,2o)	—	—	Yes

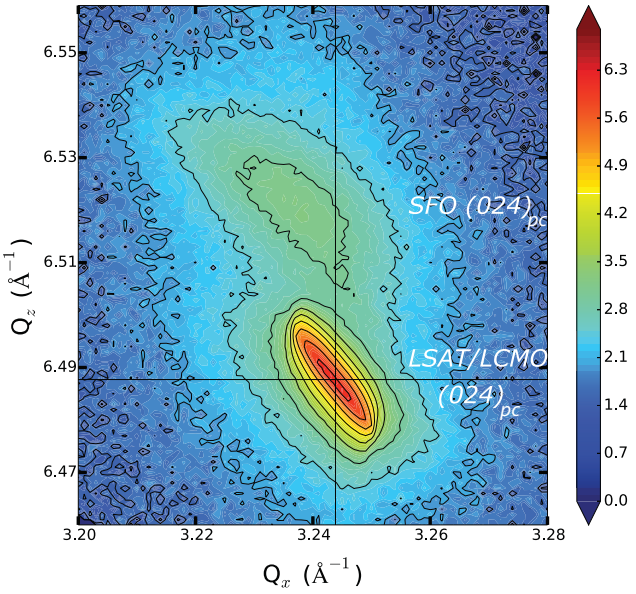

Figure 11. Reciprocal space maps around the pseudo-cubic (0 2 4) Bragg peak of a $[SFO/LCMO]_{10}$-LAO superlattice (SL1) grown on LSAT.

$0.2 \leqslant \delta \leqslant 0.1$ and orthorhombic LCMO layers for which the long-axis is pointing in the out-of-plane direction.

3.2.1.3. Epitaxy with RSM. The reciprocal space map (RSM) of the SFO/LCMO superlattice (SL1) around the pseudo-cubic (0 2 4) Bragg peak is shown in figure 11. The SFO lattice parameters derived from the RSM are aSFO = 3.885 Å (in-plane) and cSFO = 3.852 Å (out-of-plane). The c-axis of the bulk tetragonal structure of $SrFeO_{2.81}$ [41] amounts to 7.7 Å $\approx 2c_{pc}$ corresponding to a pseudo-cubic out-of-plane lattice parameter of $c_{pc} = 3.85$ Å. The in-plane lattice parameter found by the RSM analysis (3.885 Å) is slightly larger than the pseudo-cubic bulk parameter deduced from $SrFeO_{2.81}$, $a_{pc} = 10.932/\sqrt{(2)}/2 = 3.865$ Å but close to $SrFeO_{2.75}$, $a_{pc} = 10.974/\sqrt{(2)}/2 = 3.880$ Å. The LSAT lattice parameter was found to be 3.874 Å. The lattice mismatch between LSAT and LCMO is less than 0.1%, therefore the LCMO peak overlaps with the stronger LSAT Bragg peak. The lattice parameter for LCMO thus cannot be determined from the reciprocal space map.

3.2.1.4. Atomic structure with STEM. Figures 12 and 13 show the STEM ADF images of the superlattice (SL2).

The low magnification image in figure 12(a) confirms the overall high quality of this superlattice, it demonstrates that

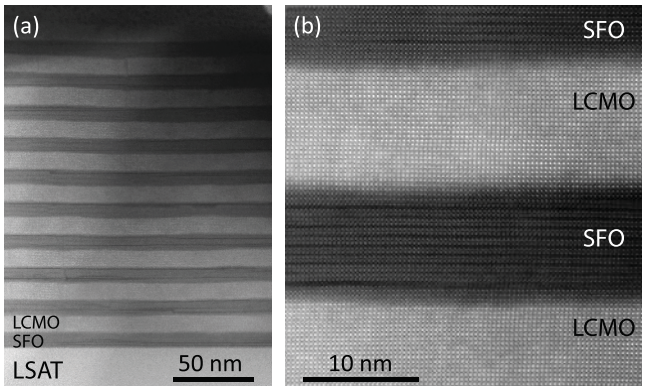

Figure 12. Low (a) and high (b) magnification ADF images of the $[SFO/LCMO]_{10}$-LAO superlattice (SL2) on LSAT.

the layers have coherent interfaces and are flat and homogeneous over long lateral distances. The LCMO layers show a brighter contrast while the SFO layers appear dark.

The high magnification image in figure 12(b) reveals that the oxygen deficient SFO layers once more exhibit characteristic dark horizontal stripes due to an oxygen vacancy ordering. These stripes are running predominantly parallel to the interface, although, occasionally they are perpendicular.

Figure 13 shows the atomic resolution chemical images of the LCMO/SFO interfaces as obtained by EELS. The yellow box in figure 13(a) highlights the region of the superlattice where the EELS spectra were collected and shows the simultaneously acquired ADF signal.

Figure 13(b) shows a set of elemental maps from the analysis of the La $M_{4,5}$, Mn $L_{2,3}$ and Fe $L_{2,3}$ absorption edges, indicated in green, red and blue, respectively. It confirms that the interfaces are chemically sharp with no sign of cation inter-diffusion. Figure 13(c) displays the averaged profiles and the atomic plane stacking at the bottom LCMO/SFO and top SFO/LCMO interfaces (with respect to the growth direction) which corresponds to MnO_2-SrO-FeO_2 for the former and FeO_2-LaO-MnO_2 for the latter. Statistically speaking, this is the predominant sequence found throughout the entire part of the sample that has been measured with STEM.

3.2.2. Magnetic properties. The magnetization of the SFO/LCMO multilayer SL1 was measured with VSM and is presented in section 3.2.2.1. We have found an intriguing exchange bias effect which is discussed in section 3.2.2.2.

3.2.2.1. DC magnetization. The magnetization data of the SFO/LCMO superlattice (SL1) shows signatures of a strong mutual influence between the SFO and LCMO layers. In

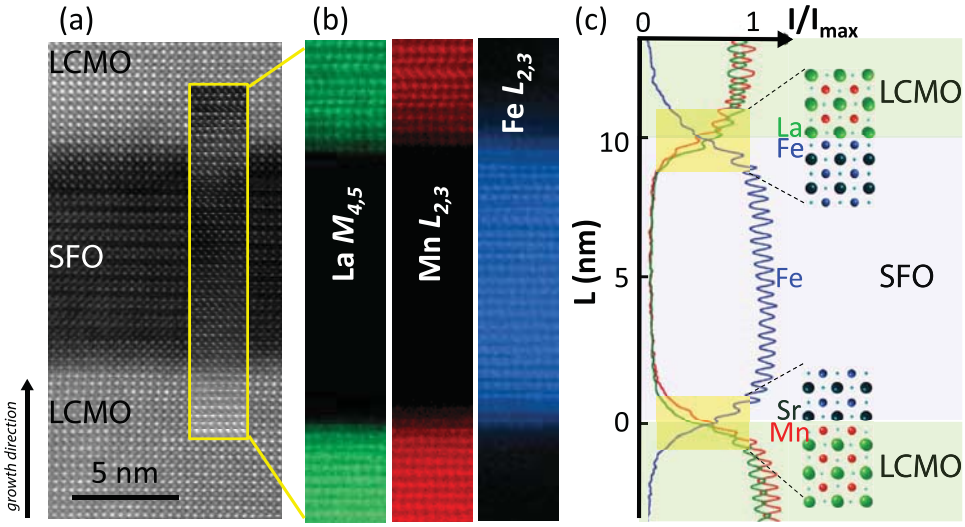

Figure 13. EELS elemental mapping of a LCMO/SFO/LCMO trilayer sequence in the SL1 superlattice. (a) Annular dark field (ADF) image. The yellow box highlights the region where the EELS data were acquired. The inset includes the ADF signal that was simultaneously acquired with the EELS data. Some spatial drift is present. (b) Atomic resolution elemental maps corresponding to the La (green), Mn (red) and Fe (blue) species. They have been obtained from the analysis of the La $M_{4,5}$, Mn $L_{2,3}$ and Fe $L_{2,3}$ edges. (c) Averaged profiles measured on the elemental images in (b), same color code. A sketch of the interface terminations is included on the right side.

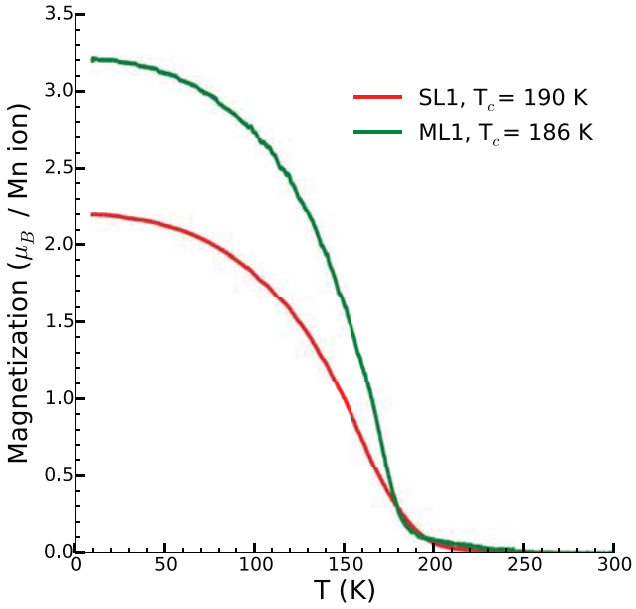

Figure 14. Magnetization versus temperature upon field-cooling in 0.1 T for the $[SFO/LCMO]_{10}$-LAO superlattice, SL1, and a LCMO (ML1) thin film.

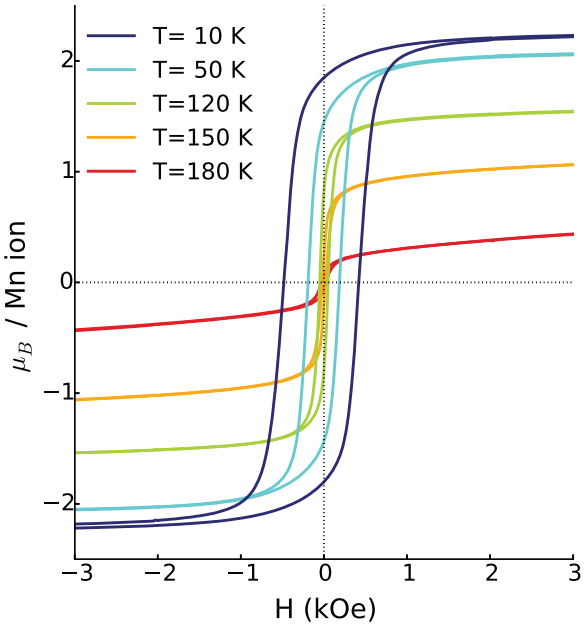

Figure 15. Magnetization versus field loops measured after field cooling in 6 Tesla for the $[SFO/LCMO]_{10}$-LAO superlattice, SL1.

particular, we observe a sizeable reduction of the average magnetic moment of the LCMO layers, a strong increase of the coercive field and a negative exchange bias effect. Figure 14 compares the T-dependent magnetization of the superlattice, SL1, and the LCMO monolayer, ML1, as measured in field-cooled mode at 0.1 T. The magnetic moment is displayed in units of Bohr magneton, μ_B, per Mn ion calculated according to

$$M_s = M/(\mu_B \cdot N) = M \cdot V_{uc}/(\mu_B \cdot A \cdot d) \qquad (1)$$

where M is the magnetic moment in emu = erg/gauss, N the number of Mn ions per LCMO unit cell, V_{uc} the unit cell volume, $\mu_B = 9.27 \times 10^{-21}$ erg/gauss the Bohr magneton, A the surface area and d the total thickness of the LCMO layer(s).

Both samples exhibit a characteristic ferromagnetic response with a spontaneous magnetization that develops below a Curie temperature of about 186 K and 190 K for ML1 and SL1, respectively. These Curie temperatures are typical for thin LCMO films [3]. The low temperature value of about 3.2 μ_B/Mn of the single LCMO layer is only moderately reduced as compared to the one in bulk LCMO single crystals for which the maximal value is around 3.7 μ_B/Mn. The corresponding magnetic moment of the superlattice SL1 is significantly lower and amounts to about 2.2 μ_B/Mn. This

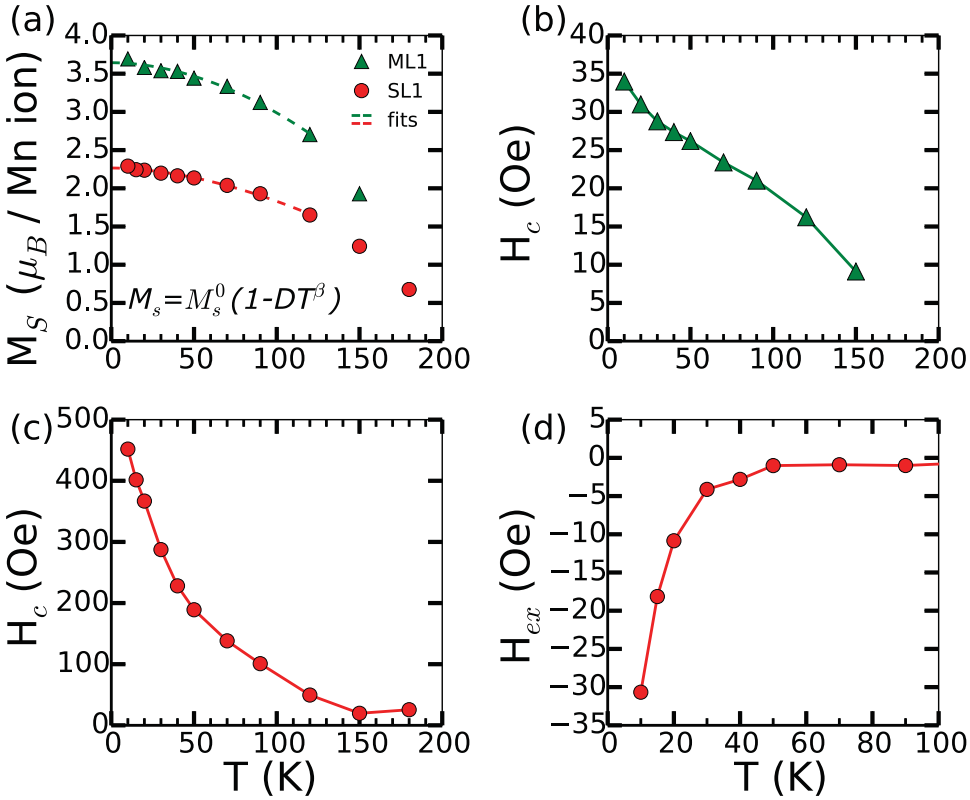

Figure 16. Parameters determined from magnetization loops after 6 T field cooling; (a) saturation moment per Mn ion for the superlattice (SL1) and the LCMO monolayer (ML1), (b) coercive field of ML1, (c) coercive field of SL1, (d) exchange bias of SL1.

may be caused by a so-called depletion layer which leads to a suppression of the FM moment in the vicinity of the LCMO/SFO interface, similar to the one that was previously found in YBCO/LCMO superlattices [5, 43, 44]. Interfacial magnetic dead layers have also been found in other ferromagnetic materials such as $La_{2/3}Sr_{1/3}MnO_3$ (LSMO) grown on various substrates [45, 46] and Fe_3O_4 grown on MgO (0 0 1) [47]. In the latter material a polar catastrophe is avoided by the magnetic dead layer [48].

3.2.2.2. Exchange bias with VSM. Figure 15 shows the magnetization loops of SL1 at several temperatures below T_c. The M–H loops have been taken in order of increasing temperature after the sample was cooled to 10 K in a field of +6 T parallel to the film plane. The shape of the M–H loops is characteristic of a FM response with a clear hysteresis at low field and a saturation toward high fields. The saturation moment, M_s, increases toward a low temperature value of about 2.25 μ_B/Mn that compares well with the one deduced from the field-cooled data at 0.1 T in figure 14. The coercive field, H_c, below which the magnetization becomes hysteretic, shows a pronounced increase toward low temperature and reaches about 450 Oe at 10 K. Notably, the M–H loop at 10 K is not centered around the field-axis but is slightly shifted toward negative fields. Such a so-called exchange bias effect arises in systems for which the ferromagnetic moments are coupled to spins that are somehow locked along a certain direction. In the present case this exchange bias effect originates most likely from the interfacial coupling between the ferromagnetic LCMO and the helimagnetic SFO layers.

Figure 16 shows a more detailed analysis of the T-dependence of M_s, H_c and H_{ex} for the LCMO monolayer (ML1) and the superlattice (SL1). Figure 16(a) details the T-evolution of M_s. Fits of the T-dependence below 120 K have been performed with the function $M_s = M_s^0(1 - DT^\beta)$ (solid lines), where M_s^0 is the extrapolated value of the saturation magnetization at 0 K and D and β describe the thermally-induced reduction of the magnetization [49–51].

The best fit parameters for the saturation moments are $M_s^0 = 3.64$ μ_B for ML1 and $M_s^0 = 2.27$ μ_B for SL1. As was mentioned before, the decreased saturation moment of the superlattice can be explained in terms of a depleted layer (with a suppressed FM order) at the LCMO/SFO interface.

Figure 16(b) shows the T-dependence of the coercive field $H_c = (H_{c+} - H_{c-})/2$ of the single LCMO film ML1. The magnitude of H_c increases toward low temperature but it remains very small and does not exceed 35 Oe at 10 K. Such a soft magnetic behavior is typical for LCMO thin films grown on substrates with a small lattice mismatch [52]. Figure 16(c) shows that the coercive field of SL1 is much larger than for ML1 and exhibits a rather steep low T upturn that sets in below about 100 K as the SFO layers develop a static magnetic order.

Figure 16(d) displays the T-dependence of the exchange bias field, $H_{ex} = (H_{c+} + H_{c-})/2$, for SL1. No exchange bias could be observed in ML1.

For SL1 there is a clear, negative exchange bias that develops below about 50 K and grows in magnitude as the temperature decreases. The onset temperature of the exchange bias around 50 K coincides with a change in the slope of the magnetoresistance, which is shown in figure 18.

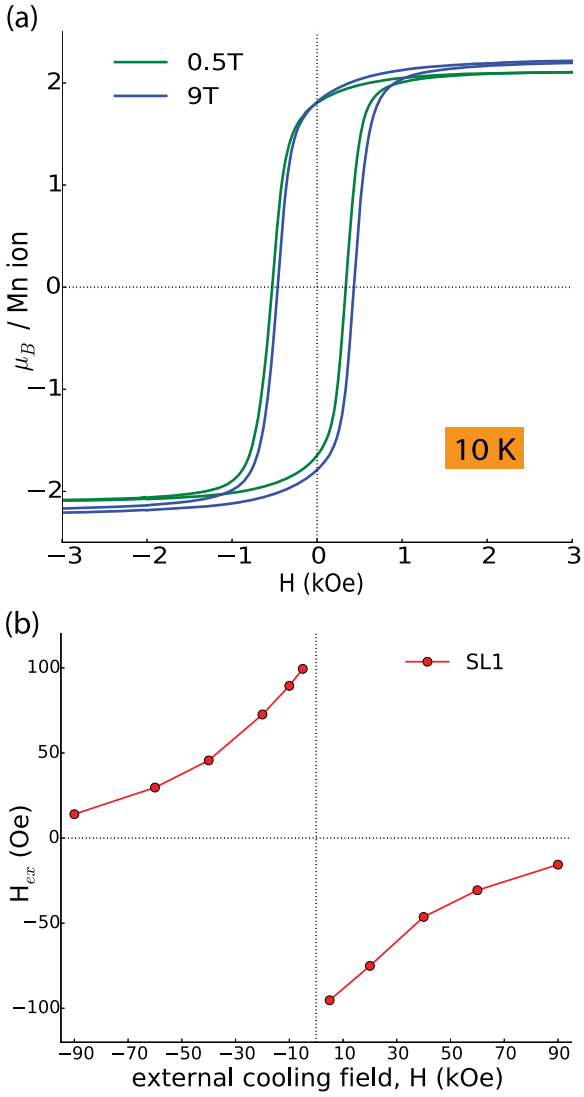

Figure 17. (a) Magnetization versus field loops at 10 K after field cooling in 0.5 and 9 T for the $[SFO/LCMO]_{10}$-LAO superlattice (SL1). (b) Exchange bias as a function of the cooling field measured at 10 K for superlattice SL1.

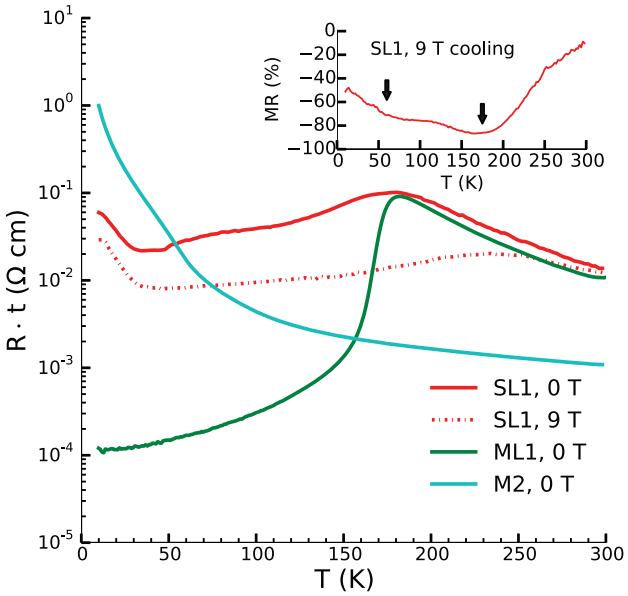

Figure 18. Resistivity versus temperature in zero field cooling for the $[SFO/LCMO]_{10}$-LAO superlattice SL1, monolayer LCMO (ML1) and SFO (M2) thin films. Inset: Magnetoresistance MR = [R(H)-R(0)]/R(0) for 9 T field cooling of SL1.

The magnitude of H_{ex} increases continuously and reaches a value of $H_{ex} = -30$ Oe at 10 K. A negative exchange bias, thus a shift of the M–H loop towards the negative magnetic field direction for positive cooling fields can occur independent of whether the coupling at the AFM/FM interface is FM or AF. Similar exchange bias effects have been observed in $BiFeO_3/La_{0.7}Sr_{0.3}MnO_3$ bilayers and superlattices [53–56], $La_{0.3}Sr_{0.7}FeO_3/SrRuO_3$ bilayers [57] and in several other systems such as $LaNiO_3/LaMnO_3$ superlattices [58] or Fe_3O_4/CoO system [59].

Figure 17 shows the dependence of the exchange bias on the cooling field for SL1. Figure 17(a) shows two M–H loops that have been measured at 10 K after cooling in different fields of 0.5 T and 9 T, respectively. Figure 17(b) shows the dependence of the exchange bias on the cooling field in more detail. It reveals that the magnitude of the negative exchange bias is much larger for the smaller cooling field. A similar dependence of the exchange bias on field cooling has been previously found in e.g. FeF_2/Fe bilayers on MgO (grown at 200 °C) and has been assigned to the AFM interaction with the magnetic field during the most recent cooling procedure [60]. This characteristic behavior of the exchange field may be understood in terms of an antiferromagnetic interfacial coupling between the Mn moments of the FM LCMO layer and the Fe moments of the SFO layer with an AF or helical magnetic order. In this case, the Mn moments of the FM LCMO layer align themselves parallel to the applied positive field, whereas the Fe moments right at the interface, that are subject to an AF exchange coupling with the Mn moments, acquire an antiparallel orientation. Note that the Néel temperature of the AF or helical order of the Fe moments is well below the Curie temperature of the FM order of the Mn moments. A larger cooling field competes with this AF interfacial coupling between the Mn and Fe moments and eventually rotates or flips the interfacial Fe moments towards a parallel orientation with respect to the field. This reduces the magnitude of the negative exchange bias and eventually should even give rise to a sign change toward a positive exchange bias. The data in figure 17 show that the field required to rotate or flip a majority of the Fe spins, as to induce such a sign change, is somewhat higher than 9 T. The AF coupling between the interfacial Fe and Mn spins thus seems to be quite strong.

3.2.3. Electronic properties. The magnetoresistance of the superlattices was measured with the 4-point probe and is discussed in the next subsection.

3.2.3.1. Magnetoresistance with 4-point probe. Figure 18 displays the resistivity curves of the SFO/LCMO superlattice (SL1) and the thin films of LCMO (ML1) and SFO (M2). All samples have been measured during zero-field-cooling, except for SL1 which has also been measured while cooling in a field of 9 T (dashed red line). The temperature-dependence of the resistance curve of the LCMO thin film (green line) shows a pronounced

change from insulator-like to metal-like state that coincides with the Curie temperature around 190 K. This transition involves a decrease of the resistance by about three orders of magnitude and arises from the competition between a Jahn–Teller distortion of the oxygen octahedra and subsequent localization of charge carriers and the so-called double-exchange interaction which yields an itinerant ferromagnetic state below T_c.

The room temperature value of the resistance of the as grown SFO film (cyan line) is lower by about an order of magnitude than the one of the LCMO film. However, the resistance of the SFO film keeps increasing toward low temperature whereas the resistance of the LCMO layer decreases sharply below T_c. Accordingly, the low-T resistivity of SFO is nearly four orders of magnitude higher than the one of LCMO.

For the SFO/LCMO superlattice it is thus expected that the T-dependence of the resistance curve is metal-like below T_c (due to LCMO) and insulator-like above T_c (due to LCMO and SFO). Such a trend is indeed observed in figure 18, albeit, the transition around T_c is considerably broader and the decrease toward low temperature is weaker than in the monolayer LCMO thin film. The resistivity for SL1 remains fairly high below T_c and even starts to increase again below 30 K. This indicates that the mobility of the charge carriers in the LCMO layers is significantly degraded as compared to the monolayer LCMO film. The inset of figure 18 shows that the SL1 also exhibits an unusual MR effect. Unlike the colossal magnetoresistance (CMR) effect in bare LCMO, which yields a sharp maximum of the negative MR around T_c, the MR of SL1 persists over a very broad temperature range and still amounts to -50% at 10 K. The MR also exhibits an additional structure around 55 K that is reminiscent of a magnetic transition of the SFO layers.

4. Conclusions

In summary, we have investigated the structural, electronic and magnetic properties of $SrFeO_{3-\delta}$ (SFO) thin films and $SrFeO_{3-\delta}/La_{2/3}Ca_{1/3}MnO_3$ (SFO/LCMO) superlattices that were grown with pulsed laser deposition (PLD) on LSAT substrates. Their high structural quality has been confirmed with x-ray diffraction and reflectometry (XRD and XRR) and scanning transmission electron microscopy (STEM) studies. The latter also revealed an interesting difference in the layer stacking sequence of MnO_2-SrO-FeO_2 at the LCMO/SFO and FeO_2-LaO-MnO_2 at the SFO/LCMO interfaces (along the PLD growth direction). The XRD data suggest that the as grown single SFO films and SFO/LCMO superlattices typically have an oxygen-deficient structure of $SrFeO_{3-\delta}$ with $\delta \leqslant 0.2$ and I4/mmm space group symmetry. For the post growth ozone annealed SFO films they are consistent with a nearly oxygen stoichiometric structure. The electronic and magnetic properties of the as-grown and ozone annealed SFO monolayers are fairly similar to the ones of $SrFeO_{3-\delta}$ ($\delta \leqslant 0.2$) single crystals. In particular, the electric transport and infrared spectroscopy showed that the as grown $SrFeO_{3-\delta}$ films are insulating whereas the ozone annealed films are metallic. The infrared data of the as grown SFO film also showed additional, sharp phonon modes that appear below 110 K and resemble the ones in the charge ordered phase of $SrFeO_{2.85}$ crystals. The magneto-resistance effects of the as grown thick SFO films are similarly large as in corresponding single crystals but they have a markedly different temperature dependence. Whereas in the SFO single crystals large MR effects occur only in the vicinity of the AF/CO phase transition around 60–70 K, in the thick SFO films a large negative MR persists to the lowest measured temperature of 10 K. Last but not least, the SFO/LCMO superlattices exhibit a rather large negative exchange bias effect that is dependent on the cooling field. These intriguing, new results call for a systematic study of the exchange-bias effect in superlattices with different thicknesses of SFO and LCMO and also direct studies of the magnetic coupling of the Fe and Mn ions at the SFO/LCMO interface.

Acknowledgments

The work at the University of Fribourg was supported by the Schweizer Nationalfonds (SNF) through grants No. 200020-153660, No. 200020-172611 and CRSII2-154410/1. Some ellipsometry measurements were performed at the IR beamline of the ANKA synchrotron at FZ Karlsruhe, where we acknowledge technical support by M Süpfle. Parts of this research, x-ray diffraction measurements, were carried out at the light source PETRA III at DESY, a member of the Helmholtz Association (HGF). The authors acknowledge funding from the MINECO (Spain) for financial support through the MAT2015-66888-C3-3-R grant and also from the ERC Proof-of-concept MAGTOOLS. We thank the Master students S Aeby and C Folly for measuring the electronic properties of some of the SFO films.

ORCID iDs

E Perret https://orcid.org/0000-0001-7543-5875

References

[1] Tokura Y 2006 *Rep. Prog. Phys.* **69** 797
[2] Millis A J, Littlewood P B and Shraiman B I 1995 *Phys. Rev. Lett.* **74** 5144
[3] Das S *et al* 2014 *Phys. Rev.* B **89** 094511
[4] Snyder G J, Hiskes R, DiCarolis S, Beasley M R and Geballe T H 1996 *Phys. Rev.* B **53** 14434
[5] Uribe-Laverde M A *et al* 2013 *Phys. Rev.* B **87** 115105
[6] Satapathy D K *et al* 2012 *Phys. Rev. Lett.* **108** 197201
[7] Nogués J and Schuller I K 1999 *J. Magn. Magn. Mater.* **192** 203
[8] Adler P, Lebon A, Damljanović V, Ulrich C, Bernhard C, Boris A V, Maljuk A, Lin C T and Keimer B 2006 *Phys. Rev.* B **73** 094451
[9] Reehuis M, Ulrich C, Maljuk A, Niedermayer C, Ouladdiaf B, Hoser A, Hofmann T and Keimer B 2012 *Phys. Rev.* B **85** 184109
[10] Lee S H, Frawley T W, Yao C H, Lai Y C, Du C H, Hatton P D, Wang M J, Chou F C and Huang D J 2016 *New J. Phys.* **18** 093033

[11] Chakraverty S *et al* 2013 *Phys. Rev.* B **88** 220405
[12] Shimakawa Y 2013 *Bull. Chem. Soc. Japan* **86** 299
[13] Chakraverty S, Ohtomo A, Okude M, Ueno K and Kawasaki M 2010 *Cryst. Growth Des.* **10** 1725
[14] Hirai K, Kan D, Ichikawa N, Mibu K, Yoda Y, Andreeva M and Shimakawa Y 2015 *Sci. Rep.* **5** 7894
[15] Solís C, Rossell M D, Garcia G, Figueras A, Van Tendeloo G and Santiso J 2008 *Solid State Ionics* **179** 1996
[16] Yamada H, Kawasaki M and Tokura Y 2002 *Appl. Phys. Lett.* **80** 622
[17] Hayashi N, Terashima T and Takano M 2001 *J. Mater. Chem.* **11** 2235
[18] Lei D Y, Kéna-Cohen S, Zou B, Petrov P K, Sonnefraud Y, Breeze J, Maier S A and Alford N M 2012 *Opt. Express* **20** 4419
[19] Sun X Y *et al* 2015 *Nanotechnology* **26** 115701
[20] Smolyaninova V N, Talanova E, Kennedy R, Kolagani R M, Overby M, Aldaco L, Yong G and Karki K 2007 *Phys. Rev.* B **76** 104423
[21] Hayward S A *et al* 2005 *Phys. Rev.* B **72** 054110
[22] Wang Y and Nastasi M (ed) 2009 *Handbook of Modern Ion Beam Materials Analysis* (Pittsburgh, PA: Materials Research Society)
[23] Chu W K, Mayer J W and Nicolet M A 1978 *Backscattering Spectrometry* (New York: Academic)
[24] Doolittle L R 1986 *Nucl. Instrum. Methods* B **15** 227
[25] Bernhard C, Humlícek J and Keimer B 2004 *Thin Solid Films* **455–6** 143
[26] Bosman M, Watanabe M, Alexander D and Keast V 2006 *Ultramicroscopy* **106** 1024
[27] Björck M and Andersson G 2007 *J. Appl. Crystallogr.* **40** 1174
[28] Hirai K, Kan D, Aso R, Ichikawa N, Kurata H and Shimakawa Y 2013 *J. Appl. Phys.* **114** 053514
[29] Lebedev O I, Verbeeck J, Van Tendeloo G, Hayashi N, Terashima T and Takano M 2004 *Phil. Mag.* **84** 3825
[30] Shimakawa Y, Inoue S, Haruta M, Kawai M, Matsumoto K, Sakaiguchi A, Ichikawa N, Isoda S and Kurata H 2010 *Cryst. Growth Des.* **10** 4713
[31] Gazquez J, Bose S, Sharma M, Torija M A, Pennycook S J, Leighton C and Varela M 2013 *APL Mater.* **1** 012105
[32] Kienle L, Adler P, Strempfer J, Keimer B, Duppel V and Phillipp F 2007 *J. Phys. Chem. Solids* **68** 73
[33] Lebon A, Adler P, Bernhard C, Boris A V, Pimenov A V, Maljuk A, Lin C T, Ulrich C and Keimer B 2004 *Phys. Rev. Lett.* **92** 037202
[34] Wagner J and Cardona M 1985 *Phys. Rev.* B **32** 8071
[35] Rice M J, Lipari N O and Strässler S 1977 *Phys. Rev. Lett.* **39** 1359
[36] Humlícek J 2011 *Thin Solid Films* **519** 2655
[37] Berkowski M, Fink-Finowicki J, Diduszko R, Byszewski P, Aleksiyko R and Kikalejshvili-Domukhovska R 2003 *J. Cryst. Growth* **257** 146
[38] Kaczmarek S M, Berkowski M, Tsuboi T, Wabia M, Wlodarski M, Olesińka W and Wrońska T 2003 *Nukleonika* **48** 35
[39] Glazer A M 1975 *Acta Cryst.* A **31** 756
[40] Woodward D I and Reaney I M 2005 *Acta Cryst.* B **61** 387
[41] Maity A *et al* 2015 *J. Phys. D: Appl. Phys.* **48** 504004
[42] Hodges J P, Short S, Jorgensen J, Xiong X, Dabrowski B, Mini S and Kimball C 2000 *J. Solid State Chem.* **151** 190
[43] Alberca A, Uribe-Laverde M A, Windsor Y W, Ramakrishnan M, Rettig L, Marozau I, Tonnerre J M, Stahn J, Staub U and Bernhard C 2015 *Phys. Rev.* B **92** 174415
[44] Sen K *et al* 2016 *Phys. Rev.* B **93** 205131
[45] Sun J Z, Abraham D W, Rao R A and Eom C B 1999 *App. Phys. Lett.* **74** 3017
[46] Moon E J, Balachandran P V, Kirby B J, Keavney D J, Sichel-Tissot R J, Schlepütz C M, Karapetrova E, Cheng X M, Rondinelli J M and May S J 2014 *Nano Lett.* **14** 2509
[47] van der Heijden P A A, Bloemen P J H, Gaines J M, van Eemeren J T W M, Wolf R M, van der Zaag P J and Jonge W J M 1996 *J. Mag. Mag. Mat.* **159** L293
[48] Chang C F *et al* 2016 *Phys. Rev.* X **6** 041011
[49] Marín L, Ramírez J G and Gómez M E 2010 *J. Phys.: Conf. Ser.* 200 072064
[50] Campillo G, Gomez M E, Berger A, Hoffmann A, Escudero R and Prieto P 2006 *J. Appl. Phys.* **99** 08C106
[51] Patel R S, Majumdar A K, Hebard A F and Temple D 2005 *J. Appl. Phys.* **97** 033910
[52] Kawashima K, Logvenov G, Christiani G and Habermeier H U 2015 *J. Magn. Magn. Mater.* **378** 539
[53] Wu S M, Cybart S A, Yu P, Rossell M D, Zhang J X, Ramesh R and Dynes R C 2010 *Nat. Mater.* **9** 756
[54] Sung K D, Lee T K and Jung J H 2015 *Nanoscale Res. Lett.* **10** 125
[55] Singh S *et al* 2014 *Phys. Rev. Lett.* **113** 047204
[56] Singh S, Xiong J, Chen A P, Fitzsimmons M R and Jia Q X 2015 *Phys. Rev.* B **92** 224405
[57] Rana R, Pandey P, Singh R P and Rana D S 2014 *Sci. Rep.* **4** 4138
[58] Gibert M, Viret M, Zubko P, Jaouen N, Tonnerre J M, Torres-Pardo A, Catalano S, Gloter A, Stéphan O and Triscone J M 2016 *Nat. Commun.* **7** 11227
[59] Ijiri Y, Schulthess T C, Borchers J A, van der Zaag P J and Erwin R W 2007 *Phys. Rev. Lett.* **99** 147201
[60] Nogués J, Lederman D, Moran T J and Schuller I K 1996 *Phys. Rev. Lett.* **76** 4624